THE ASTROPHYSICAL JOURNAL, 536:845–856, 2000 June 20

A SPECTRAL LINE STUDY OF SERPENS S68 FIRS1 REGION

JOSEPH P. MCMULLIN
NRAO, 520 Edgemont Road, Charlottesville, VA 22903;jmcmulli@nrao.edu
LEE G. MUNDY
Department of Astronomy, University of Maryland, College Park, MD 20742;lgm@astro.umd.edu
GEOFFREY A. BLAKE
Division of Geological and Planetary Sciences, Caltech 150-21, Pasadena, CA 91125;gab@csardas.gps.caltech.edu
BRUCE A. WILKING
Department of Physics and Astronomy, University of Missouri-St. Louis, St. Louis, MO 63121;brucew@newton.umsl.edu
JEFFREY G. MANGUM
NRAO, 949 N. Cherry Avenue, Tucson, AZ 85721;jmangum@nrao.edu
AND
WILLIAM B. LATTER
SIRTF Science Center/IPAC, California Institute of Technology, MS 310-6, Pasadena, CA 91125;latter@ipac.caltech.edu
Received 1999 June 15; accepted 2000 January 7

ABSTRACT

A $\lambda = 1$ mm to 3 mm study of the Serpens molecular cloud core on scales of 10′ to 10″ is presented, concentrating on the northwest condensation and the embedded sources, S68 FIRS1 and S68 N. We adopt temperatures of 25 K for the extended structure (several arcminute scale) and 35 K for the embedded sources. With these values, we use molecular line ratios and LVG statistical equilibrium calculations to derive physical properties in the region. We obtain densities between 0.4–1.2 $\times$ 10^6 cm^{-3} and an overall mass of 250–300 $M_\odot$. The majority of the mass is found in extended cloud material with two peaks of 30–45 $M_\odot$ each. Values of the molecular column densities are derived on scales of 60″–75″ (condensation) and 25″–30″ (embedded sources). The column densities in the condensation are typically as high as in the embedded sources, despite a factor of 4–5 in beam area, though there is some suggestion of mild depletions on smaller scales based on interferometric observations. Derived abundances for the region show similarities to both warmer cores and colder, dark cloud regions, with some values and ratios falling cleanly between this range of properties. Measurements of several deuterated species indicate enhanced abundances, suggesting the recent evaporation of grain mantles.

Overall, the combined properties and measured abundances suggest an intermediate state between the extremes of dark clouds and evolved warm cores like Orion KL. In general, the Serpens NW condensation appears very similar to the IRAS 16293–2422 region, which is itself an example of a cool, low-mass star-forming region with chemical tracers characteristic of hotter, higher mass regions. Our results support the suggestion that the general chemical morphology of a region is determined more by the age of the region than by its mass.

Subject headings: ISM: abundances — ISM: individual (S68) — ISM: molecules — radio continuum: ISM — stars: formation

1. INTRODUCTION TO STUDY

The diversity of chemical species present in molecular clouds provides a potentially powerful tool for deriving the physical properties of the gas and dust, and for placing constraints on the energetic processes and timescales associated with star formation (e.g., Hogerheijde et al. 1999; Blake et al. 1995; McMullin et al. 1994b; Goldsmith et al. 1992; Blake et al. 1987). However, studies of the molecular emission from young stellar objects often report an unsettling diversity of emission distributions of tracer molecules, even for those molecules that are expected to indicate similar physical characteristics. In general, the intense activity in a star-forming region (simultaneous infall and outflow, shocks, disk accretion, and photoprocesses) along with poorly characterized physical processes associated with gas-grain and grain surface interactions combine to blur the physical interpretation of the observed behavior of the molecular emission. It is therefore a challenge to understand and interpret the conduct of molecular tracers and to find sufficiently distinct and unambiguous chemical signposts for probing specific types of behavior.

Studies of the Serpens molecular cloud exemplify the problems in interpreting emission morphologies in star-forming regions. Common molecular tracers display a wide variety of behaviors in response to the complex structure resulting from the formation of a number of low-to-intermediate mass stars (e.g., Testi & Sargent 1998; Eiroa & Casali 1992). Overlapping high-velocity flows (e.g., Wolf-Chase et al. 1998; White, Casali, Eiroa 1995) and uncertainties in the opacity, radiative transfer, and excitation (e.g., Hogerheijde et al. 1999; Hurt & Barsony 1996; White et al. 1995; McMullin et al. 1994a) limit attempts to characterize the region.

In this paper, we attempt to understand the complex emission morphology of the Serpens region using a battery of observations from $\lambda = 1$–3 mm over a range of physical size scales. The observations are intended to isolate some of the many coupled effects and permit an outline of the

overall structure and characteristics of the region. The focus is on interpreting multitransitional observations to allow a derivation of the physical characteristics through statistical equilibrium radiative transfer calculations. Comparisons between the different scales of emission and with other well-studied star-forming regions are used to suggest an evolutionary "state" for Serpens.

2. OBSERVATIONS

Single-dish observations of the Serpens S68 region were obtained in the $\lambda = 3$, 2, and 1.3 mm bands with the NRAO[1] 12 m antenna and the Caltech Submillimeter Observatory (CSO[2]) 10.4 m antenna. Table 1 summarizes the molecules, transitions, velocity resolutions, and beam sizes for the observations.

The NRAO 12 m data were acquired in a series of runs from 1993 July to 1995 November, using the facility dual-polarization receivers. The spectrometer was configured to give both 100 kHz and 250 kHz resolution channels. The data were on-line calibrated to the T_R^* scale (Kutner & Ulich 1981). Our tables and maps report the data as main beam temperature, T_{MB}, using a main beam efficiency of $\eta_m^* = 0.83$ for data in the $\lambda = 3$ mm band from 1993, and $\eta_m^* = 0.95$, 0.83 and 0.58 in the $\lambda = 3$ mm, 2 mm and 1 mm bands, respectively, in 1994 and 1995.[3] The $C^{18}O$ $J = 1 \rightarrow 0$, CS $J = 3 \rightarrow 2$, H_2CO $2_{02} \rightarrow 1_{01}$, H_2CO $3_{03} \rightarrow 2_{02}$ and DCO^+ $J = 1 \rightarrow 0$ maps were made in On-The-Fly mode, scanning in R.A. The scan rates were 50″/second for the $C^{18}O$ map and 10″ s^{-1} for the other maps; the maps were sampled at one-third beam spacing in declination. The individual spectra displayed and the maps of HC_3N $J = 11 \rightarrow 10$, SO $2_2 \rightarrow 1_1$, $H^{13}CO^+$ $J = 1 \rightarrow 0$ and H_2CO $1_{01} \rightarrow 0_{00}$ were acquired using absolute position

[1] The National Radio Astronomy Observatory is operated by Associated Universities, Inc. under cooperative agreement with the National Science Foundation.

[2] The CSO is operated by the California Institute of Technology under funding from the US National Science Foundation (no. AST 90-15755).

[3] See J. G. Mangum (1997), NRAO Arizona webpage at http://www.tuc.nrao.edu.obsinfo.html.

TABLE 1

OBSERVED TRANSITIONS

Transition	Observatory	ν_{rest} (GHz)	Channel Width[a] (km s^{-1})	Beam Size (arcsec)
DCO^+ $J = 1 \rightarrow 0$	NRAO 12 m	72.039	0.42	86
DCN $J = 1 \rightarrow 0$	NRAO 12 m	72.415[b]	0.41	85
H_2CO $J_{KpKo} = 1_{01} \rightarrow 0_{00}$	NRAO 12 m	72.838	0.41	85
SO_2 $J_{KpKo} = 8_{17} \rightarrow 8_{08}$	NRAO 12 m	83.688	0.36	75
SO $J_K = 2_2 \rightarrow 1_1$	NRAO 12 m	86.094	0.35	73
$H^{13}CN$ $J = 1 \rightarrow 0$	NRAO 12 m	86.340 [b]	0.35	72
$H^{13}CO^+$ $J = 1 \rightarrow 0$	NRAO 12 m	86.754	0.35	72
$HN^{13}C$ $J = 1 \rightarrow 0$	NRAO 12 m	87.091	0.34	72
HCN $J = 1 \rightarrow 0$	NRAO 12 m	88.632 [b]	0.34	71
HNC $J = 1 \rightarrow 0$	NRAO 12 m	90.664	0.33	69
HC_3N $J = 11 \rightarrow 10$	NRAO 12 m	100.076	0.30	62
$C^{18}OJ = 1 \rightarrow 0$	NRAO 12 m	109.782	0.27	56
H_2CO $J_{KpKo} = 2_{02} \rightarrow 1_{01}$	NRAO 12 m	145.603	0.21	43
CS $J = 3 \rightarrow 2$	NRAO 12 m	146.969	0.20	43
DCO^+ $J = 3 \rightarrow 2$	CSO	216.113	0.07	32
SiO $J = 5 \rightarrow 4$	CSO	217.105	0.07	32
DCN $J = 3 \rightarrow 2$	CSO	217.239	0.07	32
H_2CO $J_{KpKo} = 3_{03} \rightarrow 2_{02}$	CSO	218.222	0.07	31
H_2CO $J_{KpKo} = 3_{03} \rightarrow 2_{02}$	NRAO 12 m	218.222	0.13	28
H_2CO $J_{KpKo} = 3_{22} \rightarrow 2_{21}$	NRAO 12 m	218.476	0.13	28
$C^{18}O$ $J = 2 \rightarrow 1$	CSO	219.560	0.07	31
DNC $J = 3 \rightarrow 2$	CSO	228.911	0.06	30
CH_3OH $J = 5 \rightarrow 4$ E	CSO	241.8	0.06	29
$H^{13}CN$ $J = 3 \rightarrow 2$	CSO	259.012	0.06	27
$H^{13}CO^+$ $J = 3 \rightarrow 2$	CSO	260.256	0.06	27
$HN^{13}C$ $J = 3 \rightarrow 2$	CSO	261.263	0.06	26
HCN $J = 3 \rightarrow 2$	CSO	265.886	0.05	26
HCO^+ $J = 3 \rightarrow 2$	CSO	267.558	0.05	26
HNC $J = 3 \rightarrow 2$	CSO	271.981	0.05	25
CS $J = 7 \rightarrow 6$	CSO	342.883	0.04	20
$H^{13}CO^+$ $J = 4 \rightarrow 3$	CSO	346.999	0.04	20
SiO $J = 8 \rightarrow 7$	CSO	347.331	0.04	20
$H^{13}CO^+$ $J = 1 \rightarrow 0$	BIMA	86.754	0.67	10.4 × 7.9
SiO $J = 2 \rightarrow 1$	BIMA	86.847	0.67	10.4 × 7.9
^{13}CO $J = 1 \rightarrow 0$	BIMA	110.201	0.53	7.3 × 5.2
$C^{18}O$ $J = 1 \rightarrow 0$	BIMA	109.782	0.53	7.3 × 5.0

[a] Cited for the 100 kHz filterbank for NRAO data; CSO spectra have been smoothed to channel widths of 0.3–0.4 km s^{-1} for display.

[b] Frequency for the $F = 2$–1 transition.

TABLE 2

RESULTS OF $\lambda = 3$ mm SPECTRAL LINE SURVEY

Transition	Position	Peak T_{MB} (K)	RMS (K)	$V_{LSR}^{a,b}$ (km s^{-1})	ΔV^b (km s^{-1})
HCN $J = 1 \rightarrow 0$	S68 FIRS1	2.12	0.08	8.1	9.4
HCN $J = 1 \rightarrow 0$	S68 N	2.19	0.12	8.9	11.0
DCN $J = 1 \rightarrow 0$ $F = 2$–1	S68 FIRS1	0.26	0.03	8.0	1.3
DCN $J = 1 \rightarrow 0$ $F = 1$–1		0.18		8.1	0.9
DCN $J = 1 \rightarrow 0$ $F = 0$–1		0.14		6.7	0.9
DCN $J = 1 \rightarrow 0$ $F = 2$-1	S68 N	0.34	0.03	8.4	1.3
DCN $J = 1 \rightarrow 0F = 1 = -1$		0.19		8.4	1.5
DCN $J = 1 \rightarrow 0$ $F = 0$–1		<0.09		...	...
HNC $J = 1 \rightarrow 0$	S68 FIRS1	2.41	0.13	8.1	2.8
HNC $J = 1 \rightarrow 0$	S68 N	2.23	0.10	8.8	3.5
$H^{13}CN$ $J = 1 \rightarrow 0$ $F = -1$	S68 FIRS1	0.32	0.04	8.6	1.9
$H^{13}CN$ $J = 1 \rightarrow 0$ $F = 1$–1		0.17		8.5	2.9
$H^{13}CN$ $J = 1 \rightarrow 0$ $F = 0$–1		0.18		8.5	1.1
$H^{13}CN$ $J = 1 \rightarrow 0$ $F = 2$–1	S68 N	0.35	0.03	8.6	2.4
$H^{13}CN$ $J = 1 \rightarrow 0$ $F = 1$–1		0.19		8.6	2.1
$H^{13}CN$ $J = 1 \rightarrow 0$ $F = 0$–1		<0.09		...	...
$HN^{13}C$ $J = 1 \rightarrow 0$	S68 FIRS1	0.54	0.06	8.6	1.2
$HN^{13}C$ $J = 1 \rightarrow 0$	S68 N	0.34	0.07	9.1	1.5
HC_3N $J = 11 \rightarrow 10$	S68 FIRS1	0.43	0.07	8.5	1.2
HC_3N $J = 11 \rightarrow 10$	S68 N	0.62	0.08	8.5	1.4
$H^{13}CO^+$ $J = 1 \rightarrow 0$	S68 FIRS1	1.62	0.07	8.5	1.5
$H^{13}CO^+$ $J = 1 \rightarrow 0$	S68 N	1.25	0.10	8.7	1.4
DCO^+ $J = 1 \rightarrow 0$	S68 FIRS1	1.83	0.11	8.9	1.3
DCO^+ $J = 1 \rightarrow 0$	S68 N	1.12	0.11	9.2	1.3
H_2CO $1_{01} \rightarrow 0_{00}$	S68 FIRS1	2.39	0.10	8.4	2.5
H_2CO $1_{01} \rightarrow 0_{00}$	S68 N	1.88	0.12	8.3	3.2
SO $J_K = 2_2 \rightarrow 1_1$	S68 FIRS1	0.87	0.04	8.8	1.3
SO $J_K = 2_2 \rightarrow 1_1$	S68 N	0.42	0.08	8.4	0.8
$C^{18}O$ $J = 1 \rightarrow 0$	S68 FIRS1	3.7	0.19	8.5	1.4
$C^{18}O$ $J = 1 \rightarrow 0$	S68 N	3.9	0.19	8.5	1.4

[a] Derived from centroid.
[b] Determined from one-component Gaussian fit to line core.

switching to a reference position 20′ W and 20′ S of S68 FIRS1. Table 2 gives the typical rms noise levels for the observations and the line parameters toward S68 FIRS1 and S68 N. The coordinates for these two positions are R.A. (J2000) = $18^h29^m49^s.8$, Decl. (J2000) = 01°15′20″, and R.A. (J2000) = $18^h29^m47^s.5$, Decl. (J2000) = 01°16′51″, respectively.

The CSO observations were obtained with the facility 230 and 345 GHz receivers from 1993 June 5–8 June and 1994 March 3–7 . Spectra were acquired toward S68 FIRS1 and S68 N. The facility 1024 channel acousto-optical spectrometers with 50 and 500 MHz bandwidth served as the back ends. The typical rms noise levels are given in Table 3. The antenna temperatures, T_A^*, were converted to main beam temperatures using $\eta_m = 0.74$ at 230 GHz and 0.62 at 345 GHz. The 500 MHz bandwidth spectrometer was not operational during the 1994 March observations.

Spectral line and continuum data toward S68 FIRS1 were also obtained using the six element BIMA array between 1993 November and 1994 January. Two configurations of the 2048 channel digital correlator were utilized; the first to observe SiO, $H^{13}CO^+$, and SO (0.34 km s^{-1} resolution), and the second to observe $C^{18}O$ and ^{13}CO (0.3 km s^{-1} resolution). In each case, the molecular lines were placed in the upper sideband to allow simultaneous continuum observations in the lower sideband at 84 and 107 GHz, respectively. Frequencies, beam sizes and typical noise values are given in Table 1. The projected antenna spacings ranged from 2 kλ to 37 kλ. The resulting naturally-weighted synthesized beams are 10″.4 × 7″.9 and 7″.3 × 5″.1 at 86 and 110 GHz, respectively. The compact source 1733-130 was used as a phase calibrator with a flux of 7.0 Jy, as derived from planetary observations.

The interferometer data were reduced with the MIRIAD[4] and AIPS++[5] software packages. A line-free continuum map was formed by averaging the channels in a correlator band showing no line emission. Spectral line maps were made by subtracting the dirty continuum maps from the dirty spectral line maps. The data were then CLEANed. No correction for primary beam taper was applied.

3. RESULTS

The following two subsections present the observations showing the structure of the region on a 10 arcminute scale, and then focus in on the structure of the northwest condensation on scales of arcminutes down to arcseconds.

3.1. *The S68 Region*

The $C^{18}O$ $J = 1$–0 emission integrated over the velocity interval 5.5 to 11.5 km s^{-1}, shown in Figure 1, traces the overall column density structure of the Serpens cloud. The

[4] Multichannel Image Reconstruction, Image Analysis, and Display software developed by the Berkeley-Illinois-Maryland Association.
[5] Astronomical Information Processing System software developed by ATNF, NFRA, NRAO, and BIMA.

TABLE 3

RESULTS OF $\lambda = 1$ AND 2 mm SPECTRAL LINE SURVEY

Transition	Position	Peak T_{MB} (K)	RMS (K)	V_{LSR}[a,b] (km s^{-1})	ΔV[b] (km s^{-1})
CS $J = 3 \rightarrow 2$	S68 FIRS1	1.6	0.08	8.4	3.0
CS $J = 3 \rightarrow 2$	S68 N	2.2	0.08	8.2	4.0
DCO^+ $J = 3 \rightarrow 2$	S68 FIRS1	0.81	0.09	8.4	1.1
DCO^+ $J = 3 \rightarrow 2$	S68 N	0.73	0.06	8.9	1.4
SiO $J = 5 \rightarrow 4$	S68 FIRS1	0.15	0.06	8.2	3.5
SiO $J = 5 \rightarrow 4$	S68 N	0.21	0.04	6.9	10.9
DCN $J = 3 \rightarrow 2$	S68 FIRS1	0.20	0.04	8.7	1.2
DCN $J = 3 \rightarrow 2$	S68 N	0.20	0.04	3.8	5.9
H_2CO $2_{02} \rightarrow 1_{01}$	S68 FIRS1	1.1	0.16	8.7	3.1
H_2CO $2_{02} \rightarrow 1_{01}$	S68 N	1.2	0.16	8.2	4.6
H_2CO $3_{03} \rightarrow 2_{02}$	S68 FIRS1	0.74	0.06	8.8	2.7
H_2CO $3_{03} \rightarrow 2_{02}$	S68 N	1.68	0.05	7.8	5.2
$C^{18}O$ $J = 2 \rightarrow 1$	S68 FIRS1	5.47	0.06	8.7	1.8
$C^{18}O$ $J = 2 \rightarrow 1$	S68 N	4.24	0.04	8.7	1.6
SO_2 $1_{11} \rightarrow 0_{10}$	S68 FIRS1	...	0.05	...	...
SO_2 $1_{11} \rightarrow 0_{10}$	S68 N	...	0.05	...	...
DNC $J = 3 \rightarrow 2$	S68 FIRS1	0.27	0.04	8.3	1.3
DNC $J = 3 \rightarrow 2$	S68 N	0.26	0.05	8.6	1.5
CH_3OH $J_K = 5 \rightarrow 4$ E	S68 FIRS1	0.46	0.08	8.4	1.7
CH_3OH $J_K = 5 \rightarrow 4$ A	S68 FIRS1	1.52	0.14	8.4	1.9
$H^{13}CN$ $J = 3 \rightarrow 2$ $F = 2$–1	S68 FIRS1	0.24	0.08	8.7	2.5
$H^{13}CN$ $J = 3 \rightarrow 2$ $F = 2$–1	S68 N	0.22	0.11	8.8	3.1
$H^{13}CO^+$ $J = 3 \rightarrow 2$	S68 FIRS1	1.49	0.11	8.7	2.0
$H^{13}CO^+$ $J = 3 \rightarrow 2$	S68 N	...	...	...	...
$HN^{13}C$ $J = 3 \rightarrow 2$ $F = 2$–1	S68 FIRS1	0.35	0.06	8.1	1.3
$HN^{13}C$ $J = 3 \rightarrow 2$ $F = 2$–1	S68 N	...	0.05	...	...
HCN $J = 3 \rightarrow 2$	S68 FIRS1	1.29	0.13	9.8	12.2
HCN $J = 3 \rightarrow 2$	S68 N	1.28	0.11	6.9	8.9
HCO^+ $J = 3 \rightarrow 2$	S68 FIRS1	3.61	0.14	9.3	6.9
HCO^+ $J = 3 \rightarrow 2$	S68 N	3.05	0.11	8.0	4.6
HNC $J = 3 \rightarrow 2$	S68 FIRS1	0.53	0.07	8.6	3.2
HNC $J = 3 \rightarrow 2$	S68 N	1.23	0.07	8.8	1.9
CS $J = 7 \rightarrow 6$	S68 FIRS1	2.82	0.25	8.8	3.0
CS $J = 7 \rightarrow 6$	S68 N	1.26	0.23	7.0	5.3

[a] Derived from centroid.
[b] Determined from one-component Gaussian fit to line core.

backbone of the cloud is an arc curving through roughly 180°, with a length of 30′. Two main peaks in the $C^{18}O$ emission are located near the center of the arc, separated by 4′. The peak line temperatures in the channel maps are 4–5 K, and the integrated emission peaks, over a velocity interval of ± 3 km s^{-1} from ambient, are 8–9 K km s^{-1} . Submillimeter (Casali, Eiroa, & Duncan 1993) and far infrared (Hurt & Barsony 1996) continuum emission from the region are dominated by sources that lie primarily in the region between the two $C^{18}O$ peaks and to the northwest of the northern $C^{18}O$ peak. The triangles in Figure 1 show the positions of the six submillimeter peaks detected by Casali et al. (1993). A cluster of 50–140 young stars lies in the area of, and 1′–2′ north of, the group of four submillimeter sources to the southeast in Figure 1 (Eiroa & Casali 1992).

One striking feature of the $C^{18}O$ emission is its lack of correspondence with the submillimeter emission peaks. The $C^{18}O$ and submillimeter dust continuum emission are both tracers of column density, but with different dependences on temperature. Thus temperature variations seriously affect the relative distributions of these two traditional column density tracers (see Wilson et al. 1986). This point will be followed up quantitatively in § 4.2.

A first moment map of the $C^{18}O$ emission (Fig. 2) displays a broad velocity gradient running from a velocity centroid of 9.0 km s^{-1} at the northwest end of the emission to 7.5 km s^{-1} at the southeast end. This corresponds to a velocity gradient of roughly 2 km s^{-1} pc^{-1}. It is unclear if this gradient arises from rotation, two clouds at different velocities, or interaction of cloud material with the recent star formation.

Maps of the H_2CO $2_{02} \rightarrow 1_{01}$, H_2CO $3_{03} \rightarrow 2_{02}$ CS $J = 3 \rightarrow 2$, and DCO^+ $J = 1 \rightarrow 0$ emission from a smaller region around the infrared sources are shown in Figure 3. The six submillimeter peaks identified by Casali et al. (1993) are labeled in the lower right panel. The peak SMM1 is better known as S68 FIRS1 and we will use that designation in this paper. The peak SMM6 can be identified with SVS20, the brightest near infrared source in the area (Eiroa & Casali 1992). All four of the transitions in Figure 3 have higher critical densities than $C^{18}O$ and hence are better tracers of the high-density gas distribution. Very similar structure can be seen in the CS and H_2CO emission. The two peaked structure is broadly similar to that of $C^{18}O$ but the peaks are more accentuated and located along the northern or eastern edges of the $C^{18}O$ peaks. The southern peak in CS and H_2CO is coincident with the submillimeter source SMM4 (Eiroa & Casali 1992) and the northern peak

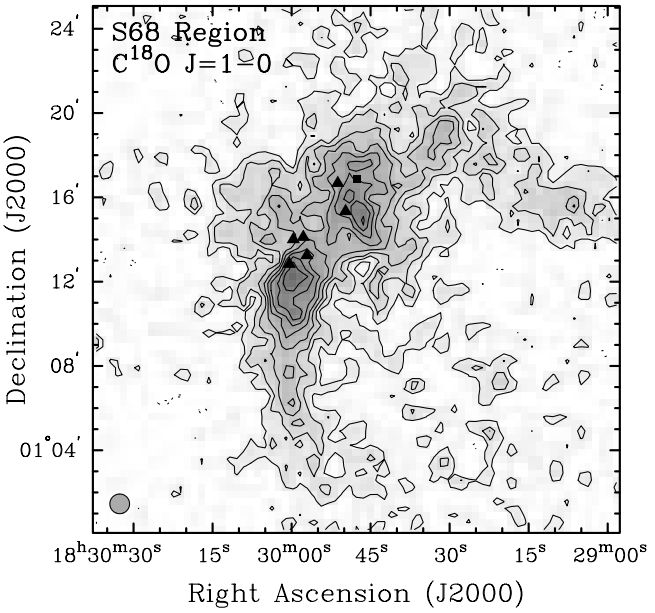

FIG. 1.—Integrated $C^{18}O$ $J = 1$–0 emission from the Serpens S68 region. The emission is integrated from 5.5 to 11.5 km s^{-1}. The contour intervals are in steps of 1 K km s^{-1} starting at 1 K km s^{-1}; the highest peak in the map is 8.8 K km s^{-1}. The triangles denote the positions of the submillimeter emission peaks enumerated by Casali et al. (1993). The square marks the position of S68 N (McMullin et al. 1994a). The beam size is given in the lower left corner.

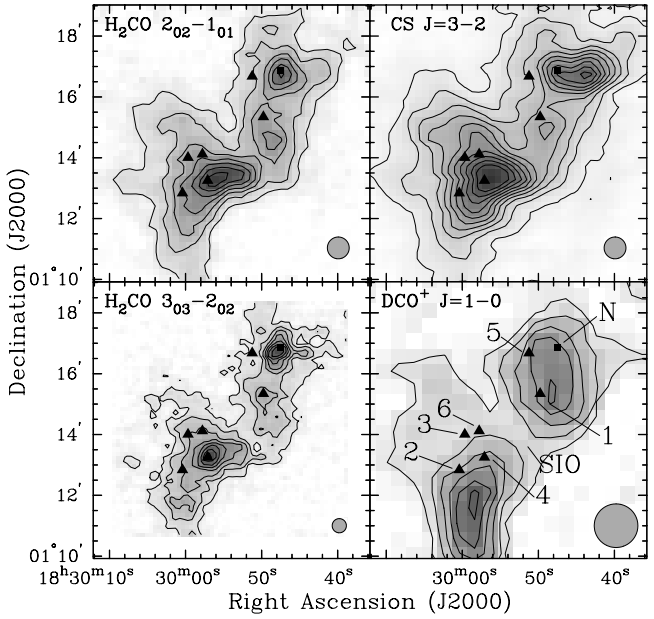

FIG. 3.—Maps of the integrated emission from the H_2CO $2_{02} \rightarrow 1_{01}$, CS $J = 3 \rightarrow 2$, H_2CO $3_{03} \rightarrow 2_{02}$, and DCO^+ $J = 1 \rightarrow 0$ transitions. The contour levels in the maps are 1.0, 1.0, 0.8, and 0.5 K km s^{-1}, respectively. The beams for the observations are given in the lower right corner and in Table 1. As in Fig. 1, the triangles mark the locations of the SMM sources and the square marks the position of S68 N. The numbers assigned to the SMM peaks by Casali et al. (1993) are shown in the lower right panel.

can be identified with the source S68N (marked by a square in the figures) (McMullin et al. 1994a). The DCO^+ emission follows the structure seen in $C^{18}O$ more closely than that seen in CS or H_2CO. This may be because the DCO^+ $J = 1 \rightarrow 0$ line is more easily excited than the CS or H_2CO transitions and because the DCO^+ is selectively formed in cold molecular gas.

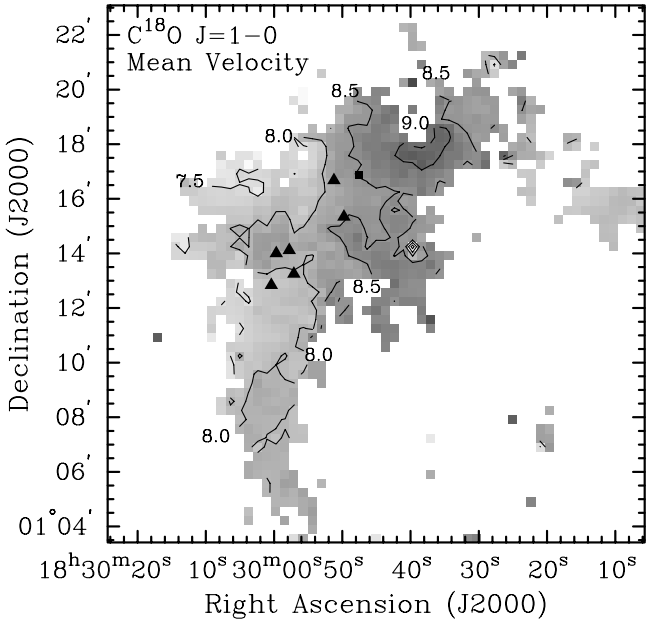

FIG. 2.—Mean velocity map derived from the $C^{18}O$ $J = 1 \rightarrow 0$ data. The gray scale and contours display the mean velocity (first moment of the emission) in units of km s^{-1}. The numbers label the velocities of the nearby contours.

3.2. *The S68 Northwest Condensation*

We will refer to the area around S68 FIRS1, SMM5, and S68 N collectively as the northwest condensation. Maps of the integrated HC_3N $J = 11 \rightarrow 10$, SO $J_K = 2_2 \rightarrow 1_1$, $H^{13}CO^+$ $J = 1 \rightarrow 0$, and H_2CO $1_{01} \rightarrow 0_{00}$ emission from the northwest condensation are shown in Figure 4. The emission distributions are extended and generally peak near S68 FIRS1 (*lower triangle*). The small spatial offsets between the emission peaks and S68 FIRS1 are within the pointing uncertainties. All of the distributions are elongated in the direction of S68 N (*square*), but none show distinct peaks at that location. The SMM5 position does not feature prominently in any of the transitions in Figures 1, 3, or 4.

Figure 5 displays a selection of $\lambda = 3$ mm spectra toward S68 FIRS1 and S68 N. Self-absorptions are clearly present at the cloud velocity in HCN and HNC. The line profiles for the isotopic and deutrated species typically have FWHM's of 1.4 km s^{-1}, while the main species lines are 2–3 km s^{-1} wide, reflecting the optical depths in those transitions. Table 2 summarizes the measured line parameters.

Maps of the integrated $C^{18}O$ $J = 2 \rightarrow 1$, HCO^+ $J = 3 \rightarrow 2$, HCN $J = 3 \rightarrow 2$, and $H^{13}CO^+$ $J = 3 \rightarrow 2$ emission from the northwest condensation are shown in Figure 6. The $C^{18}O$ $J = 2$–1 emission is strong throughout the region and traces the overall condensation with a weak peak toward S68 FIRS1, in overall agreement with the $C^{18}O$ $J = 2 \rightarrow 1$ map of White et al. (1995). The emission distributions of the HCO^+, HCN, and $H^{13}CO^+$ $J = 3 \rightarrow 2$ transitions are quite different from the low -J transitions in Figures 1, 3, and 4. The high-J emission reveals discrete peaks associated with S68 FIRS1 and S68 N. This is most obvious in the HCN and HCO^+ maps; the $H^{13}CO^+$ emission peaks on S68 FIRS1, but is incompletely sampled in the regions of S68 N. This behavior is also evident in the

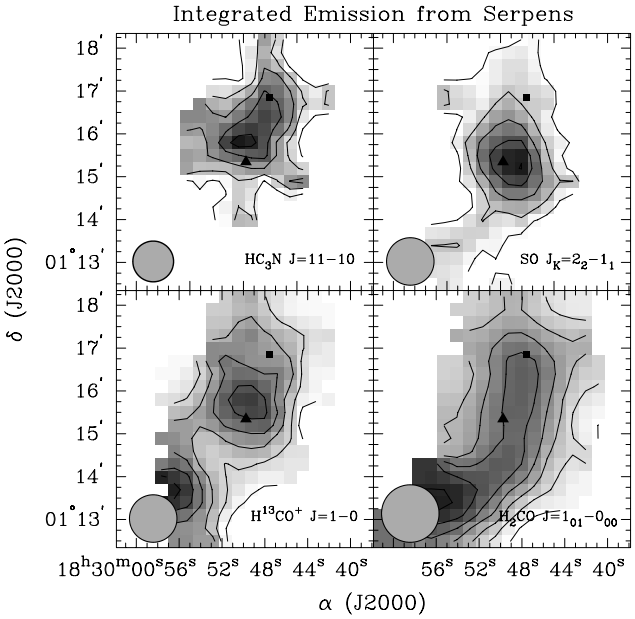

FIG. 4.—Integrated emission from HC_3N $J = 11 \rightarrow 10$, SO $2_2 \rightarrow 1_1$, $H^{13}CO^+$ $J = 1 \rightarrow 0$, and H_2CO $1_{01} \rightarrow 0_{00}$ transitions toward the Serpens northwest condensation Contour levels are in steps of 0.15, 0.2, 0.4, and 1.0 K km s^{-1} for HC_3N, SO, $H^{13}CO^+$, and H_2CO, respectively. The solid triangle marks the millimeter continuum position for S68 FIRS1; the solid box marks S68 N. Beams are shown in the lower left of each panel and the beam sizes are given in Table 1.

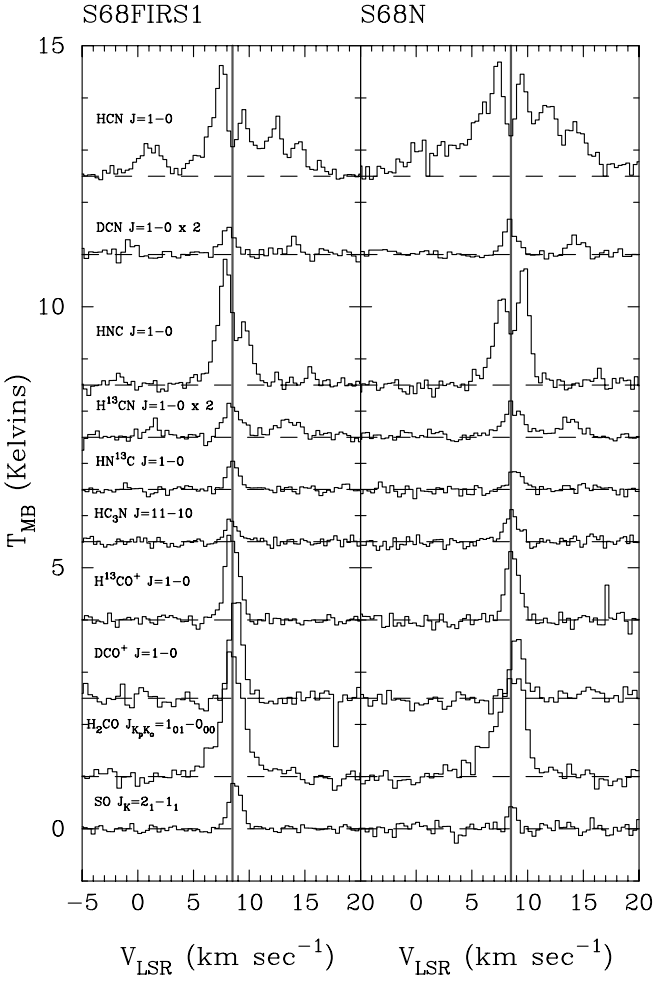

FIG. 5.—Spectra toward S68 FIRS1 (the peak continuum position) and toward S68 N. The gray lines mark $V_{LSR} = 8.5$, the nominal cloud velocity. The molecular species and transition for each spectrum is identified in the left column. The vertical scale is in units of main beam brightness temperature. The spectral are all on the same scale but have been offset vertically for display.

HCO^+ $J = 4 \rightarrow 3$ map by White et al. (1995) and in the higher J maps of Hogerheijde et al. (1999), which show strong molecular peaks associated with the embedded sources. The offset between the S68 N position and the HCN and HCO^+ peaks (also the H_2CO $3_{03} - 2_{02}$ peak in Fig. 3) is likely real. The shift, about 12″ southeast, places the emission closer to a peak in the 12 and 25 μm emission (Hurt & Barsony 1996); it is within the contours of an unlabeled peak in the 1100 μm map (Casali et al. 1993) and close to a 3 mm peak found by Testi & Sargent (1998).

Individual spectra in the $\lambda = 1$ mm band toward S68 FIRS1 and S68 N are shown in Figures 7 and 8. Broad-line wings, indicative of outflow activity, are obvious in the HCO^+, H_2CO, HCN, and CS lines. DCN also shows a weak, very broad line toward S68 N, while SiO shows a broad profile toward both S68 FIRS1 and S68 N. Self-absorption and distorted line shapes are obvious in transitions of common molecules, such as HCN, HCO^+, and H_2CO. The $H^{13}CO^+$ line in Figure 7 is actually stronger at line center than the HCO^+ line and, at its maximum, the HCO^+ line is only twice as strong as the peak in the $H^{13}CO^+$ line. Similarly, the HCN/$H^{13}CN$ and HNC/$HN^{13}C$ line ratios indicate significant optical depths in the main isotopes as found by Hogerheijde et al. (1999). Table 3 summarizes the line parameters for these observations.

Interferometer maps of the integrated $C^{18}O$ $J = 1 \rightarrow 0$, ^{13}CO $J = 1 \rightarrow 0$, $H^{13}CO^+$ $J = 1 \rightarrow 0$, and SiO $J = 2 \rightarrow 1$ emission toward S68 FIRS1 are given in Figure 9. The $C^{18}O$ emission peaks weakly on the S68 FIRS1 continuum source position. The $H^{13}CO^+$ emission peaks on S68 FIRS1 and is extended a little to the northwest and to the east. The SiO emission shows two peaks 10–15″ to the south of S68 FIRS1. This emission is in the direction of the blue wing peak in SiO from single dish maps (McMullin et al. 1994a) but that peak is outside the interferometer's field of view. No ^{13}CO $J = 1 \rightarrow 0$ emission was detected toward S68 FIRS1; however, strong systematic effects were present in the data, which rendered it problematic. This combined with the high line opacity in the extended condensation will resolve out flux in the remaining visibilities. Maps of these transitions were also obtained by Hogerheijde et al. (1999) with the OVRO interferometer. These maps are very similar for $C^{18}O$ and $H^{13}CO^+$ both in intensity and distribution. However the SiO emission appears extended at a somewhat different position angle in our maps (along an outflow lobe rather than along the axis of the condensation). In addition, ^{13}CO was detected with OVRO as a broad self-absorbed line.

Spectra based on the BIMA channel maps are displayed in Figure 10. The left column shows spectra toward S68 FIRS1; the right column contains spectra toward the peak position for each individual molecule. Clearly, the emission mapped by the interferometer is not peaked at the V_{LSR} of the single-dish lines (*shaded line*). At the S68 FIRS1 position, the ^{13}CO, $C^{18}O$, and $H^{13}CO^+$ lines all peak 1–2 km s^{-1} to the blue of the ambient cloud velocity, which is a little beyond the half-power line width of the single dish

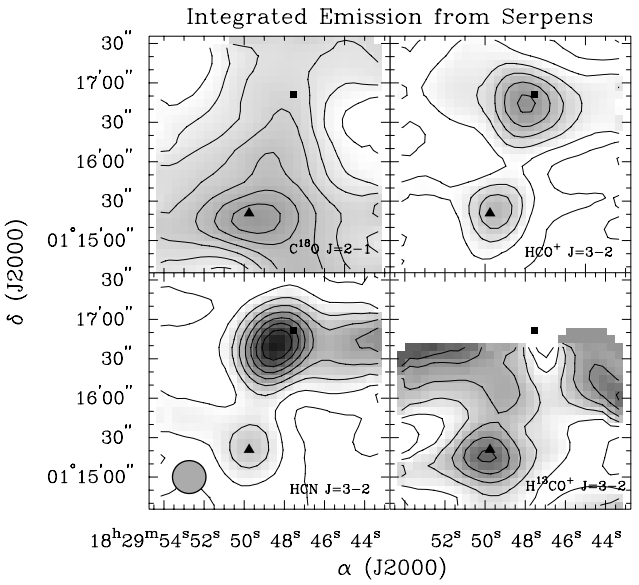

FIG. 6.—Integrated emission in the $C^{18}O$ $J = 2 \rightarrow 1$, HCO^+ $J = 3 \rightarrow 2$, HCN $J = 3$–2, and $H^{13}CO^+$ $J = 3$–2 transitions. Contours are in steps of ± 1 K km s^{-1} for HCN and HCO$^+$ (the contours for the HCN emission start at 3 K km s^{-1}); contours are in steps of 0.2 K km s^{-1} for $H^{13}CO^+$ and in steps of 0.5 K km s^{-1} for $C^{18}O$ (starting at 4 K km s^{-1}). Symbols are the same as in Fig. 4.

lines. At the positions of peak emission for each molecule, only the SiO emission is centered on the cloud velocity; for other molecules, the observed emission is generally within 2 km s^{-1} of ambient velocity. The flux in all of these lines

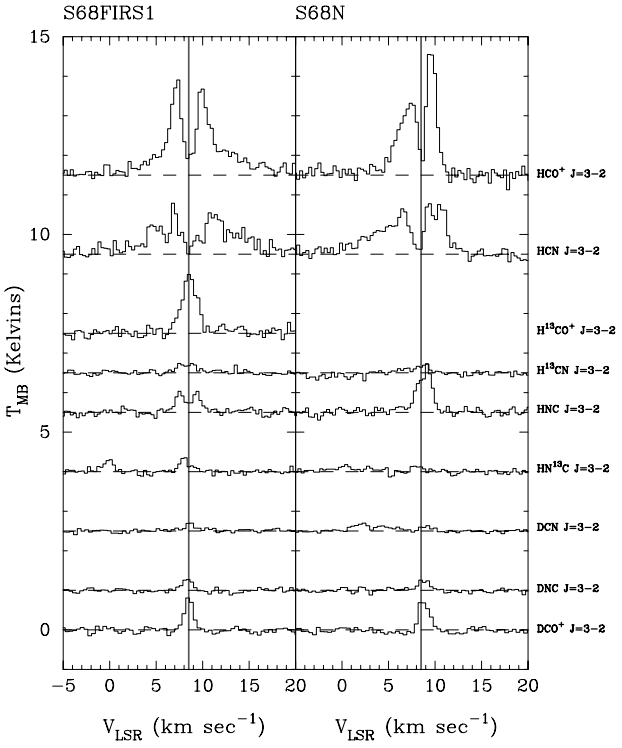

FIG. 7.—Spectra in the $\lambda = 1$ mm band toward S68 FIRS1 and S68 N from the CSO. The gray lines mark $V_{LSR} = 8.5$ km s^{-1}, the nominal cloud velocity. The vertical scale is in units of main beam brightness temperature. The molecular species and transition for each spectrum is given to the right of the right panel.

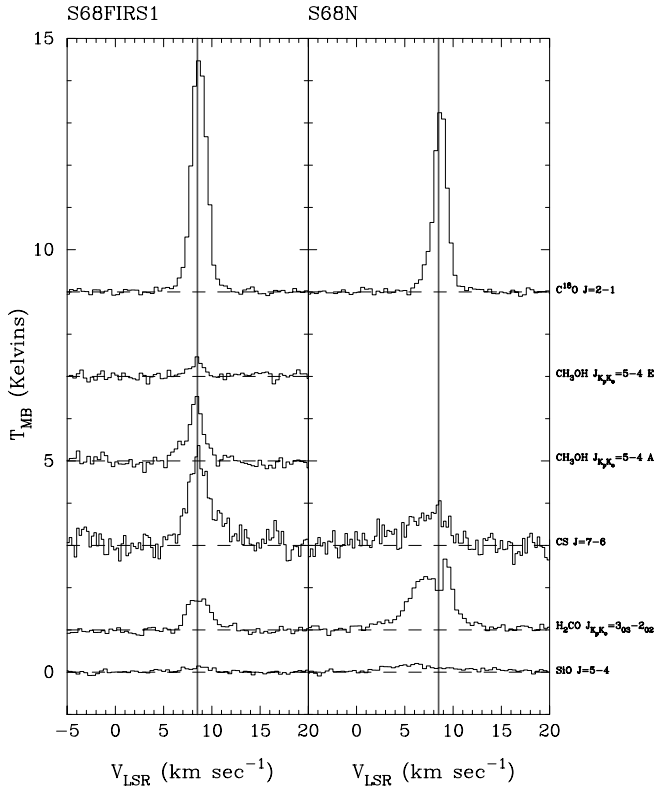

FIG. 8.—Spectra in the $\lambda = 1$ mm band toward S68 FIRS1 and S68 N. The layout of the figure is the same as for the previous figure.

represents a small fraction of the measured single dish flux. For example, the $C^{18}O$ and $H^{13}CO^+$ $J = 1 \rightarrow 0$ lines have fluxes of 90 Jy beam^{-1} and 40 Jy beam^{-1}, respectively, toward FIRS1 in the NRAO 12 m beam so the interferometer observations represent roughly 5% and 15% of the flux, respectively. Opacity drives the large amount of resolved

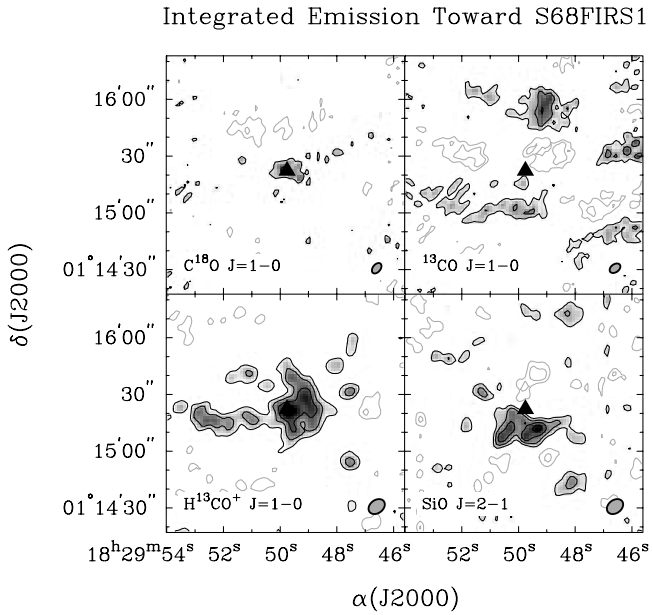

FIG. 9.—Integrated interferometer maps toward S68 FIRS1. Contour levels are in steps of ± 1.5, 1.5, 0.8, and 0.8 Jy beam^{-1} km s^{-1}, for ^{13}CO, $C^{18}O$, SiO, and $H^{13}CO^+$, respectively. The peak continuum position is marked by a solid triangle. Beams are displayed in the lower left.

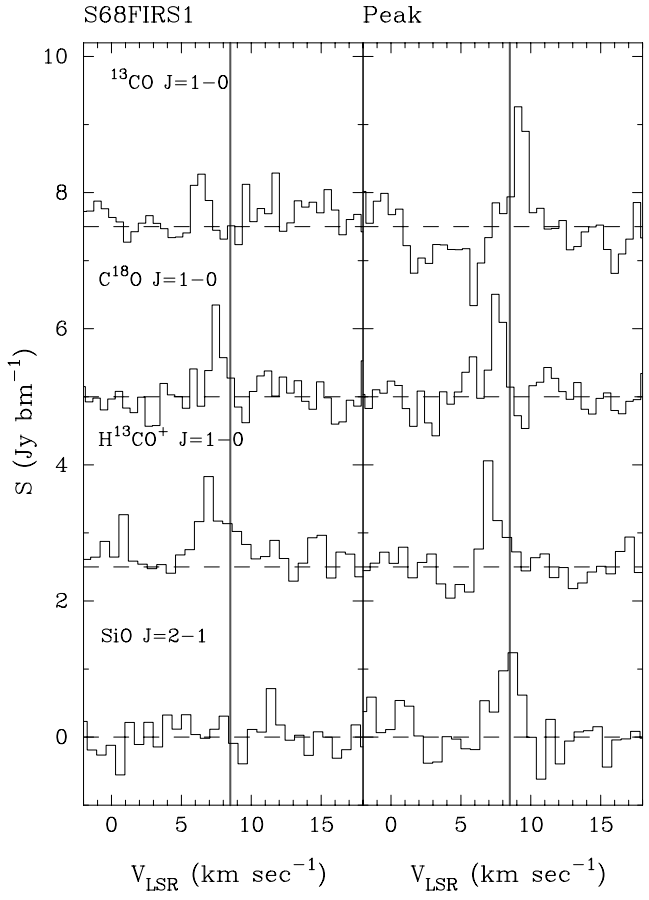

FIG. 10.—Spectra toward S68 FIRS1 (the peak continuum position) and toward the molecular emission peak of each molecule. The gray lines mark the location of the $V_{LSR} = 8.5$ km s^{-1}, the nominal cloud velocity.

out flux (Hogerheijde et al. 1999), and results in the observed shift in that the bulk of the emission cannot be seen, only the material traced by the redshifted or blueshifted gas.

A continuum map, made from the 107 GHz interferometer data, shows a peak flux density of 188 mJy beam^{-1}, which is comparable to our previous measurement at 95 GHz (140 mJy beam^{-1}; McMullin et al. 1994a). The emission is spatially coincident with the previous measurement and is unresolved in our beam.

4. UNDERSTANDING THE EMISSION MORPHOLOGIES

The morphologies of the molecular emission from the S68 region are shaped by the physical density structure (which affects the molecular excitation), the physical column density structure, the molecular abundance variations (which are driven by chemical processes, shock interactions and molecular depletions), and the kinetic temperature variations. Understanding and disentangling these causes and their effects is not possible with the data set presented here, or with the current limited understanding of molecular cloud structure. In the following sections, we use the data to outline the overall structure of the S68 region and derive some average properties for different subregions.

4.1. *The Large-Scale Cloud*

The C^{18}O emission in Figure 1 primarily traces the column density and mass structure of the S68 region. Integrating over the entire area, the total C^{18}O emission in Figure 1 corresponds to 602 K km s^{-1}. Boxes around the southern and northern C^{18}O peak regions yield 71 K km s^{-1} and 77 K km s^{-1}, respectively. Hence, roughly 75% of the C^{18}O emission arises from the extended cloud in low-level emission (emission at the 1 to 3 contour level in Figure 1).

To derive values for the column density and mass, we use Large Velocity Gradient (LVG; e.g., de Jong et al. 1975) statistical equilibrium calculations, assuming that the C^{18}O emission is optically thin, and adopting a gas temperature and density (see White et al. 1995 for a discussion of LVG versus LTE). We estimated the average gas temperature and density as follows. Far infrared emission on the scale of 1′–2′ from sources in the region have been fitted with dust temperatures of 22–35 K (McMullin et al. 1994a; Hurt & Barsony 1996; Zang, Laureijs, & Clark 1988). Such measurements are weighted toward the vicinities of embedded sources and probably overestimate the average gas temperature. The molecular gas temperatures in the region have been estimated as 25–27 K based on 2′ resolution CO observations (Loren et al. 1979) and 12–18 K based on NH_3 lines (Ungerechts & Güsten 1984; Curiel et al. 1996). White et al. (1995) estimate gas temperatures of 35–40 K over the main C^{18}O emission regions based on the peak CO line temperatures, but they argue that the larger scale cloud is probably cooler, $\sim$15 K. We adopt gas temperatures of 30 K toward the column density peaks and 20 K for the overall cloud. The gas density has been estimated as $\sim 10^6$ cm^{-3} in the vicinity of the infrared sources (McMullin et al. 1994a; Hurt, Barsony, & Wootten 1996), but the average cloud material is likely to be much lower density (White et al. 1995); we adopt the typical densities found in large-scale clouds, 2×10^3 to 10^4 cm^{-3} (Lada, Strom, & Myers 1993). With these values, the C^{18}O column density peaks of 8–9 K km s^{-1} correspond to C^{18}O column densities of $N(C^{18}O) = 7\text{–}10 \times 10^{15}$ cm^{-2}, where this range encompasses the column densities derived using the above density range. For a C^{18}O fractional abundance of 1.5×10^{-7} (C^{18}O/H$_2$ (Frerking, Langer, & Wilson 1982; van Dishoeck et al. 1993; Lada et al. 1994) and a distance of 220 pc (Festin 1998), this translates to $N(H_2) = 4\text{–}7 \times 10^{22}$ cm^{-2} or a mass of 3–5 $M_\odot$ in the beam.

Using the same assumptions, except a temperature of 20 K, the total mass of the C^{18}O $J = 1 \rightarrow 0$ emission region is 250–300 $M\odot$. With the higher temperature of 30 K for the peak regions, their masses correspond to 30–45 $M\odot$ each. These mass estimates are significantly less than that of (White et al. 1995), even though the present observations cover a larger area. The $J = 1 \rightarrow 0$ transition should be a more reliable mass tracer than the $J = 2 \rightarrow 1$ transition used by White et al. because the $J = 1 \rightarrow 0$ emission is less sensitive to density and has a factor of 2–3 less opacity. Our derived column densities and masses would be roughly a factor of 2 larger if we had used an LTE analysis.

4.2. *Physical Conditions in the Northwest Condensation*

The data are sufficient to constrain the physical conditions in the northwest condensation. Since all molecular tracers have some combination of dependences on density, temperature, and column density, one needs to start by focusing on one of the relevant quantities. The gas temperature is considered first, before moving on to the remaining properties.

The gas temperature can be estimated from the relative intensities of the observed H_2CO 3_{03}–2_{02} and 3_{22}–2_{21} transitions (Mangum & Wootten 1993) if the optical depth is modest. Optically thin analysis of this line ratio in our data suggest gas temperatures in the range of 35–70 K toward SMM4, FIRS1, and S68 N. Unfortunately, the H_2CO 3_{03}–2_{02} line profiles are flat-topped, and partially self-absorbed, suggesting significant optical depth despite the weak line temperatures. Optical depth effects preferentially cause this line ratio to mimic higher gas temperatures as the 3_{03}–2_{02} becomes saturated. Previous analysis of H_2CO data from the region yielded gas temperatures of 40–190 K (Hurt et al. 1996), although they also noted that optical depth effects could cause their values to be overestimated. Temperatures toward S68 FIRS1 and S68 N have also been derived previously from the far infrared emission, yielding dust temperatures of 23–35 K (McMullin et al. 1994a; Hurt & Barsony 1996; Zanget al. 1988). Analysis of NH_3 data toward FIRS1 find a gas temperature of 30 K in its immediate vicinity (Curiel et al. 1996). Thus, gas temperatures are probably 30 K or greater toward both S68 FIRS1 and S68 N. It is likely that both regions have internal heating sources, and hence temperature gradients and warm temperatures on small scales. For the remainder of this section, we adopt an overall gas temperature of 25 K for the northwest condensation and 35 K toward S68 FIRS1 and S68 N.

The average physical densities for the northwest condensation can be derived using the low-abundance molecular species for which we observed several transitions. For this analysis, we have used the LVG approximation to model the measured line temperatures. In order to maintain similar spatial resolutions, the high-frequency observations were smoothed to match the resolution of the $\lambda = 3$ mm data. For the three species with two or more observed transitions that are likely to be optically thin, $H^{13}CO^+$, SiO, and DCN, we derive $n(H_2) = 0.4$–1.2×10^6 cm^{-3}. The upper end of the derived density range is somewhat larger than the density derived from previous $C^{34}S$ McMullin et al. (1994a) and H_2CO Hurt et al. (1996) data, but this may be due to a higher critical density of the $H^{13}CO^+$ transitions. The values derived from DCN and SiO are more consistent with previous measurements, though their spectral characteristics are quite different (see previous section).

Table 4 lists the molecular column densities derived for the overall northwestern condensation (on 60″–75″ scales) assuming a gas temperature of 25 K, and the column densities within $\sim$ 25″–30″ beams centered on S68 FIRS1 and S68 N assuming a gas temperature of 35 K. The molecular column densities are reported as a range of values, calculated using an LVG code, with densities that span the range derived above. The isotopic species were assumed to have the same collision cross sections and dipole moments as the parent isotopomers. The dipole moments and rotation constants for the linear molecules were obtained from the line catalogue of Poynter & Pickett (1997). Values in Table 4 with lower limits indicate transitions that are optically thick. The derived column densities for HCO^+ and HCN are consistent with previous estimates in similar beams McMullin et al. (1994a), while CH_3OH has a lower column density than previously derived from a smaller beam observation.

Surprisingly, in the northwest condensation, the S68 FIRS1 and S68 N positions show very similar column densities. The range in the derived column densities is larger for the S68 FIRS1 and S68 N positions than for the overall NW condensation primarily because of the different transitions used to derive the values. The NW condensation values were derived using primarily low-J transitions whose level populations are not very sensitive to density over the range $n = 0.4$–1.2×10^6 cm^{-3}. For the S68 FIRS1 and S68 N positions, higher J transitions, whose level populations were sensitive to density, were utilized. But, in most cases, the derived column density for the northwestern condensation is within the range of values derived for S68 FIRS1 and S68 N, despite the factor of 4–5 difference in beam area sampled by the NW condensation values versus the other two. The only exception is the DCO^+ column density, which decreases by a factor of 4–6 in the smaller beams, as expected for a tracer sensitive to cold, low-density gas.

TABLE 4

MOLECULAR COLUMN DENSITIES[a]

Molecule	NW Condensation[b] (cm^{-2})	S68 FIRS1[c] (cm^{-2})	S68 N[d] (cm^{-2})
$C^{18}O$	7.0-9.0(15)	7.4–7.6(15)	5.7–5.8(15)
HCN	>3.3(13)	>6.0(13)	>4.5(13)
$H^{13}CN$	1.9–2.1(12)	2.0–5.8(12)	2.2–7.0(12)
DCN	1.2–1.4(12)	1.4–3.4(12)	1.4–3.4(12)
HNC	>1.0(13)	>6.4(12)	>9.1(12)
$HN^{13}C$	1.0–1.3(12)	1.6–5.5(12)	...
DNC	...	0.9–2.4(12)	0.9–2.6(12)
HCO^+			
$H^{13}CO^+$	3.2–4.2(12)	2.5–5.1(12)	...
DCO^+	4.5–6.4(12)	0.7–1.1(12)	0.8–1.3(12)
CS	>3.0(13)	>1.4(14)	>1.2(14)
$C^{34}S$	2.9–3.7(12)	2.6–5.7(12)	...
SiO	2.7–3.0(12)	1.4–4.4(12)	0.6–1.7(13)
p-H_2CO	>3.0(13)	...	...
p-$H_2^{13}CO$	0.9–1.1(12)	...	...
HC_3N	2.4–2.7(12)	...	...

[a] Notation for column densities is a(ba(b) = $a \times 10^b$.
[b] 60″–80″ beam centered on S68 FIRS1.
[c] 25″–32″ beam centered on S68 FIRS1.
[d] 25″32″ beam centered on S68 N.

Peak molecular column densities can also be derived from the interferometric observations. Assuming the same temperature and density conditions as for the S68 FIRS1 position above, peak column densities in $C^{18}O$, SiO, and $H^{13}CO^+$ are 1.8–2.0×10^{16}, 1.6–2.2×10^{13}, and 2.2–2.8×10^{13} cm^{-2}, respectively. The $C^{18}O$ and $H^{13}CO^+$ peaks coincide with S68 FIRS1, but, as noted previously, the SiO peak is offset significantly to the southeast. The $C^{18}O$ column density toward S68 FIRS1 is a factor of 2–3 greater in the interferometer beam than in the 30″ beam, and the $H^{13}CO^+$ column density is a factor of 5–10 greater, even though the interferometer data are recovering a small fraction of the single-dish line flux. A detailed analysis of the physical structure in the envelope by Hogerheijde et al. (1999) suggests that given the temperature and density gradients in the region, the small amount of recovered flux in CO is consistent with emission from the condensation or with mild depletions of factors 3–10. The $H^{13}CO^+$ does appear to be depleted relative to the condensation scales by a factor of at least $\sim$3.

The beam-averaged H_2 column densities toward the NW condensation and S68 FIRS1 were estimated from $\lambda = 1.25$ mm observations by McMullin et al. (1994a). An error was made in that paper (it is reported correctly in the table) in

the H_2 column density for the 60″ smoothed beam; the correct numbers are 5×10^{22} cm^{-2} for the column density in a 60″ beam and 1.2×10^{23} cm^{-2} in a 30″ beam, for a mass opacity $\kappa = 0.1(\nu/1200\ \mathrm{GHz})^{\beta}$ with $\beta = 2$. Using the same opacity law, the interferometer continuum data indicate a column density of 5×10^{24} cm^{-2} in a 6″ beam toward S68 FIRS1. Hence, the H_2 column density seems to rise quickly in the smaller beams, whereas the molecular column densities increase slowly. The $N(C^{18}O)$ is nearly unchanged between the 60″ and 30″ beams and only modestly increased in the 6″ beam, reflecting the weakness of the observed peaks in the $C^{18}O$ emission. If the emissivity law is changed from $\beta = 2$ to $\beta = 1$ at the smaller scales (in the 6″ beam), then the H_2 column density only rises by a factor of several going from 30″ scales to 6″ scales.

The observed line strength and the LVG models indicated that the $C^{18}O$ lines are not optically thick, so either the $C^{18}O$ abundance decreases at the column density peaks or, perhaps, temperature gradients drive down the apparent $N(C^{18}O)$. Addressing the later possibility, the column densities derived from the continuum and $C^{18}O$ data would show the same percentage increase between the northwestern condensation and the S68 FIRS1 position if we adopted a temperature of 50 K, rather than 35 K, in the 30″ beam. A gas temperature of 50 K can not be ruled out. However, this temperature dependence in the derived column densities can not bridge the gap between the continuum and $C^{18}O$ column densities derived for the 6″ beam. In addition, the lines in the interferometer data have intrinsically different shapes. If the fractional abundance implied for the condensation, $X(C^{18}O = 1.6 \times 10^{-7}$, applied to gas in the 6″ beam, the $C^{18}O$ lines would be optically thick in that beam and the expected flux would be $9\,(T/35\ \mathrm{K})(r_s/3'')^2$ Jy beam^{-1}, where T is the gas temperature and r_s is the source radius. Hence, with our noise level, emission from a source that is 1″ or larger in radius would have been detected, so mild depletions in CO are supported as suggested by Hogerheijde et al. (1999).

4.3. *Comparison of Relative Molecular Abundances*

Table 5 displays the abundances of the main isotopic species relative to CO for the three Serpens regions. The relative abundances, except for that of DCO^+ and SiO, do not change by more than a factor of 2 between the three locations. The fourth and fifth columns in Table 4 give the relative abundances for the young embedded source IRAS 16293-2422 and the Orion Molecular Ridge around the IRc2 position. The abundances for the S68 regions are generally similar to those of IRAS 16293-2422, with the exception of HCN, HNC, HCO^+, and DCO^+. Below we discuss a few specific cases along with their chemical interpretations.

The HNC abundance in the Serpens regions is comparable with that in the Orion Ridge, but the HCN/HNC abundance ratio is not. For Serpens, HCN/HNC is 1.1 to 1.6, whereas this ratio is 5.5 for IRAS 16293-2422 and 8 for the Orion Ridge. Abundance ratios of 2.5–6 are found in translucent clouds (Turner, Pirogov, & Mihn 1997) and $\frac{1}{3}$ to $\frac{1}{2}$ in the TMC1 cloud (Pratap et al. 1997). Thus, the Serpens HCN/HNC ratio is between that found toward TMC 1 where the gas temperature is 10 K and the Orion Ridge where the gas temperature is $\sim$40 K. This finding fits with the chemical model proposed by Schilke et al. (1992) where the HCN/HNC ratio is determined primarily by neutral-neutral reactions with significant activation energies. Our ratio is roughly consistent with their steady state model with $n = 10^6$ cm^{-3} and gas temperature of 30–35 K. The nitrogen chemical network of Turner et al. (1997) also predicts HCN/HNC$\sim$1 in dense clouds; in their model, the ratio is determined by reactions involving H_3^+. Comparing with the time dependent models of Bergin et al. (1997), we find that the HCN/HNC ratio can also be fitted with either an early time (10^5 yr), high C/O (C/O = 0.6) model or with a later time (3×10^6 yr), higher C/O (C/O = 1.0) model. Both time-dependent models provide a poor match to the absolute abundance of HCN and HNC, while the steady state models provide values closer to 5×10^{-9} (within a factor of a few).

Again, the HCO^+ relative abundance in the Serpens region is closer to that of the Orion Ridge than of IRAS 16293-2422. This may be the result of a general higher ion abundance in the Serpens and Orion regions due to active intermediate mass star formation. Increased H_3^+ abundance would drive the HCN/HNC ratio to unity (Turner et al. 1997) and increase the HCO^+ abundance since $H_3^+ + CO \rightarrow HCO^+$ is a major formation path for HCO^+.

TABLE 5

FRACTIONAL ABUNDANCES RELATIVE TO CO[a]

Molecule	NW Condensation	S68 FIRS1	S68 N	IRAS 16293[b]	Orion Ridge[c]
CO	1.0	1.0	1.0	1.0	1.0
HCN[d]	2.4–3.6(5)	3.2–9.4(−5)	4.6–15.(−5)	1.8(−5)	2.0(−4)
DCN	2.6–4.0(−7)	3.7–9.2(−7)	4.8–12.(−7)	5.6(−7)	
HNC[d]	1.3–2.2(−5)	2.5–8.9(−5)	...	3.3(−6)	1.5(−5)
DNC	...	2.3–6.5(−7)	3.1–9.1(−7)	2.2(−7)	
HCO^+[d]	4.2–7.2(−5)	3.9–8.3(−5)	...	1.0(−5)	4.0(−5)
DCO^+	1.0–8(−6)	1.8–3.0(−7)	2.8–4.6(−7)	4.4(−7)	
CS[e]	1.5–2.4(−5)	1.6–3.5(−5)	...	2.5(−5)	1.0(−4)
SiO	6.0–8.6(−7)	3.7–12.(−7)	2.0–6.0(−6)	6.9(−7)	
p-H_2CO[e]	1.2–1.9(−5)	...	...	5.8(−6)[f]	
HC_3N	5.4–7.8(−7)	...	...		6.0(−6)

[a] Derived from $N(C^{18}O)$ assuming $CO/C^{18}O = 500$.
[b] From van Dishoeck et al. 1995 and Blake et al. 1994.
[c] Average of 1.7' N and 1.3' S from Ungerechts et al. 1997.
[d] Derived from ^{13}C species assuming $^{12}C/^{13}C = 60$.
[e] Derived from ^{34}S species assuming $^{32}S/^{34}S = 23$.
[f] Derived from total H_2CO assuming o-H_2CO/p-$H_2CO = 3$.

Deuterated species give another insight into the chemical state of the gas. Table 6 summarizes the relative abundances of deuterated molecules with respect to their main isotopic species. For comparison, Table 6 also lists ratios for TMC1, IRAS 16293-2422, and warm clouds. All species show deuterium enhancements within the range found in other clouds. The DCN/HCN ratio is essentially the same for the three Serpens regions. The value falls between that found for TMC1 (a prototypical cold cloud) and warm clouds and is roughly the same as for IRAS 16293-2422, which can be characterized as a cold cloud with low-mass star formation. The chemical model proposed by Schilke et al. (1992) for HCN and HNC also predicts the DCN/HCN ratio; for the steady state model with $n = 106$ cm^{-3}, the observed ratio occurs for a temperature of 40–50 K, which is warmer than the temperature needed to match our HCN/HNC ratio.

The other ratios of deuterated and parent species in Table 6 also show interesting behavior. The DNC/HNC ratio is similar to that found in warm clouds. The DCO^+/HCO^+ ratio in the NW condensation is larger than that found in any of the other regions, while the ratio toward S68 FIRS1 is intermediate between that for IRAS 16293-2422 and warm clouds. The difference in the DCO^+/HCO^+ ratio between the NW condensation and S68 FIRS1 is clearly present in the line ratios; in the NW condensation the DCO^+ line is 50% stronger than the $H^{13}CO^+$ line, whereas toward S68 FIRS1 the DCO^+ line is only 60% of the strength of the $H^{13}CO^+$ line, a factor of 2.5 change in relative strength. For species also obtained by Hogerheijde et al. (1999), we find the derived values are consistent, generally within a factor of 2.

4.4. *The Evolutionary State of the S68 Region*

The S68 molecular cloud is not a simple region in a *single* evolutionary state. The presence of a partially unveiled young stellar cluster (Eiroa & Casali 1992), multiple molecular outflows (Wolf-Chase et al. 1998; White et al. 1995), and embedded sources with a range of spectral energy distributions (Hurt et al. 1996) is indicative of an underlying range in stellar ages. The relative distributions of the stars and warm dust and gas suggest that star formation occurred earlier at the location of the near infrared cluster and is occurring currently to the west and southwest of the cluster, as previously concluded by Hurt et al. (1996).

The northwest condensation associated with FIRS1 and S68 N is one of the regions of current star formation. We propose that the northwest condensation is an example of an intermediate type of cloud core, a cool core, which is generally intermediate in cloud properties and star formation characteristics between cold cores and warm cores (though some properties/abundances span the range of values). Such cool cores are associated with the formation of small groups of low-to-intermediate mass stars. Several lines of argument for the intermediate properties of the northwest condensation are given in the next two paragraphs.

The relative molecular abundances in the northwest condensation and around FIRS1 and S68 N are intermediate to those found in cold and warm cores. The HNC/HCN, DCN/HCN, and DNC/HNC ratios suggest that the dense gas has been heated to 25–35 K for a sufficient time for the chemistry to respond (chemical steady state is approached after $\sim$several times 10^5 years, assuming a density of 10^6 cm^{-3} and a fractional ionization of $\sim 10^{-8}$). The variation in the DCO^+/HCO^+ ratio between the FIRS 1 region and the northwest condensation shows that this heating has not occurred uniformly throughout the condensation. The DCO^+ $J = 1$–0 emission is generally peaked away from the heating sources and away from the high-density gas, suggesting that the DCO^+ abundance is high in cool lower density gas away from the star formation activity (Bergin et al. 1999; Loren et al. 1990).

The line profiles associated with the northwest condensation also suggest intermediate properties between those of dark clouds and warm cores. The line widths are typically 1.5 to 2 km s^{-1} for Serpens compared to typical 0.5 to 1 km s^{-1} line widths for dark clouds or 2 to 5 km s^{-1} for warm cores. In addition, the extreme amounts of self absorption in lines of common molecular species is characteristic of calculated microturbulent line profiles (Leung et al. 1978), which are more typical of dark cores.

Overall these properties fall between *or span* the range of values found in the extremes of cold dark clouds and warm cores, showing similarities to regions with very different masses and luminosities. The absence of any strong depletions (a signpost of youth) and the similar abundances to the more evolved Orion core suggest a more advanced age than some other embedded sources (e.g., NGC 1333 IRAS 4, Blake et al. 1995) as had been suggested for IRAS 16293-2422 (van Dishoeck et al. 1995). This finding suggests that the evolutionary state may be relatively more important than the properties of mass and luminosity which are more typically compared.

The lack of variation in abundances over a range of scales from the embedded sources to the surrounding condensation may be taken as a signpost for this stage of evolution; only on the smallest scales probed by the interferometer are there remaining indications of small amounts of depletion. In Serpens, despite the changes wrought on our observed scales, there coexist regions of extreme youth (e.g., Williams & Myers 1999). The level of star-forming activity in the region and the range of evolutionary stages present may provide vital clues to the propagation of star formation in molecular cores.

TABLE 6

RELATIVE ABUNDANCES OF DEUTERATED SPECIES

Ratio	TMC1[a]	IRAS 16293-2422[b]	NW Cond.	S68 FIRS1	S68 N	Warm Clouds[a]
DCN/HCN [c]	0.023	0.013	0.011	0.010	0.009	0.004
DNC/HNC [c]	0.015	0.03	...	0.008	...	0.01
DCO^+/HCO^+ *c*.....	0.015	0.009	0.019	0.005	...	0.002

[a] From van Dishoeck et al. 1993.
[b] From van Dishoeck et al. 1995.
[c] Obtained from the ^{13}C isotope assuming $^{12}C/^{13}C = 60$.

5. SUMMARY

We have presented a $\lambda = 1$–3 mm spectral line study of the northwest condensation of the Serpens molecular cloud core on scales from 30′ to 6″. $C^{18}O$ $J = 1$–0 emission traces a high column density arc, curving through 180° and 30′ in extent; the majority of the emission arises from low-level emission from extended cloud material. The total mass of the cloud is determined to be between 250–300 $M_\odot$ with two peaks of 30–45 $M\odot$ each.

The physical conditions in the cloud were determined from multitransition observations and an LVG radiative transfer code. A temperature of 25 K was used for the northwestern condensation and 35 K for the embedded sources, S68 FIRS1 and S68 N. We obtain a density range of 0.4–1.2 $\times$ 10^6 cm^{-3}. Using these temperatures and densities, molecular line column densities are obtained on 60–75″ and 25–30″ scales. The column densities in the northwestern condensation are typically as high as in the embedded objects, despite a factor of 4–5 difference in beam area; DCO^+ is the exception, decreasing by a factor of 4–6 in the smaller beams.

Derived relative abundances show no discernible variation between the northwestern condensation and the embedded objects on 5500 AU scales; some evidence for depletions are seen on smaller scales (2200 AU) in $C^{18}O$ and $H^{13}CO^+$; Comparison between the Serpens abundances and other molecular regions reveal general similarity with the IRAS 16293-2422 star-forming region, with the exception of HNC, HCO^+, and DCO^+. HNC and HCO^+ are more consistent with the Orion Ridge, possibly as a result of the higher activity and temperature in the region. All of the deuterated species are enhanced with respect to warm core regions, suggesting liberation of deuterated species from grain materials. Within the existing paradigm for the evolution of emission morphologies, Serpens appears to fall between the youngest class 0 sources and more evolved regions, as indicated by the similar abundances for the embedded sources and surrounding condensation. The similarities between the Orion Ridge and with IRAS 16293-2422, reaffirm the conclusions of van Dishoeck et al. (1995) that the mass of the object is secondary to age effects insofar as the chemistry is concerned.

We would like to thank all of the individuals whose help was essential for obtaining the observations necessary for this project, in particular, A. "Taco" Zalaam for help with the CSO observations and P. Hart for light-speed tuning at the 12 m. We also thank Mary Barsony, Robert Hurt, Ronak Shah, Barry Turner, and Al Wootten for interesting discussions of this region, and our anonymous referee for productive comments and questions. This work was sponsored by National Science Foundation grant AST 91-13716 and by NASA grant 01526442. G. A. B. acknowledges additional support provided by NASA (NAG 5-4383).

REFERENCES

Bergin, E. A., Goldsmith, P. F., Snell, R. L., & Langer, W. D. 1997, ApJ, 482, 285
Bergin, E. A., Plume, R., Williams, J. P., & Myers, P. C. 1999, ApJ, 512, 724
Blake, G. A., Sutton, E. C., Masson, C. R., & Phillips, T. G. 1987, ApJ, 315, 621
Blake, G. A., Sandell, G., vanDishoeck, E. F., Groesbeck, T. D., Mundy, L. G., & Aspin, C. 1995, ApJ, 441, 689
Blake, G. A., et al. 1994, ApJ, 428, 620
Casali, M. M., Eiroa, C., & Duncan, W. D. 1993, A&A, 275, 195
Curiel, S., Rodriguez, L. F., Gomeź, J. F., Torrelles, J. M., Ho, P. T. P., & Eiroa, C. 1996, ApJ, 456, 677
de Jong, T, Chu, S., & Dalgarno, A. 1975, ApJ, 199, 69
Eiroa, C., & Casali, M. M. 1992, A&A, 262, 468
Festin, L. 1998, A&A, 336, 883
Frerking, M. A., Langer, W. D., & Wilson, R. W. 1982, ApJ, 262, 596
Goldsmith, P. F., Margulis, M., Snell, R. L., & Fukui, Y. 1992, ApJ, 385, 522
Hogerheide, M. R., van Dishoeck, E. F., Salverda, J. M. 1999, ApJ, 513, 350
Hurt, R. L., & Barsony, M. 1996, ApJ, 460, L45
Hurt, R. L., Barsony, M., & Wootten, A. 1996, ApJ, 456, 686
Kutner, M. L., & Ulich, B. L. 1981, ApJ, 250, 341
Lada, C. J., Lada, E. A., Clemens, D. P., & Bally, J. 1994, ApJ, 429, 694
Lada, E., Strom, K., & Myers, P. 1993, in Protostars and Planets III, ed. Levy, E. H., Lunine, J. I., & Matthews, M. S. (Tucson: Univ. Arizona Press), 245
Leung, C. M. 1978, ApJ, 225, 427
Loren, R. B., Evans, N. J. II, & Knapp, G. R. 1979, ApJ, 234, 932
Loren, R. B., Wootten, A., & Wilking, B. A. 1990, ApJ, 365, 269L
Mangum, J. G., & Wootten, A. 1993, ApJS, 89, 123
McMullin, J. P., Mundy, L. G., & Blake, G. A. 1994a, ApJ, 437, 305
McMullin, J. P., Mundy, L. G., Wilking, B. A., Hezel, T., & Blake, G. A. 1994b, ApJ, 424, 222
Pratap, P., Dickens, J. E., Snell, R. L., Miralles, M. P., Bergin, E. A., Irvine, W. M., & Schloerb, F. P. 1997, ApJ, 486, 862
Poynter, R. L,. & Pickett, H. M. 1984, Submillimeter, Millimeter, and Microwave Spectral Line Catalogue, JPL Publication 80-23, Rev. 2 (Pasadena: JPL)
Schilke, P., Walmsley, C. M., Pineau des Forêts, G., Roueff, E., Flower, D. R., & Guilloteau, S. 1992, A&A, 256, 595
Testi, L., & Sargent, A. I. 1998, ApJ, 508, L91
Turner, B. E., Pirogov, L., & Minh, Y. C. 1997, ApJ, 483, 235
Ungerechts, H., & Gušten, R. 1984, A&A, 131, 177
van Dishoeck, E. F., Blake, G. A., Draine, B. T., & Lunine, J. I. 1993, in Protostars and Planets III, ed. Levy, E. H., Lunine, J. I., & Matthews, M. S. (Tucson: Univ. Arizona Press), 163
VanDishoeck, E. F., Blake, G. A., Jansen, D. J., & Grossbeck, T. D. 1995, ApJ, 447, 760
White, G. J., Casali, M. M., & Eiroa, C. 1995, A&A, 298, 594
Williams, J.P., & Myers, P.C. 1999, ApJ, 518, L37
Wilson, T. L., Serabyn, E., Henkel, C., & Walmsley, C. M. 1986, A&A, 158, L1
Wolf-Chase, G. A., Barsony, M., Wootten, H. A., Ward-Thompson, D., Lowrance, P. J., Kastner, J. H., & McMullin, J. P. 1998, ApJ, 501, L193
Zhang, C. Y., Laureijs, R. J., & Clark, F. O. 1988, A&A, 196, 236